ACS OMEGA

http://pubs.acs.org/journal/acsodf

Article

First-Principles Study of Induced Magnetism in Tungsten Vanadium Selenide Alloys for Spintronic Applications

Khondker Shihabul Hoque and Ahmed Zubair*

Cite This: *ACS Omega* 2022, 7, 36184−36194

Read Online

ACCESS | Metrics & More | Article Recommendations | Supporting Information

ABSTRACT: The possibility of inducing magnetization in tungsten selenide monolayer by alloying with vanadium selenide was investigated through first-principles calculations. Electronic, optical, and magnetic properties of different $W_{1-x}V_xSe_2$ alloy compositions were studied extensively. As the proportion of vanadium atoms in the alloys increased, a phase transition from semiconducting to metallic to semiconducting was discovered. All alloy compositions demonstrated induced magnetism with a long-range ferromagnetic order. Interestingly, in the case of the $W_{0.25}V_{0.75}Se_2$ alloy, spin-up states in the band diagram showed a finite band gap, while a nonzero band gap was found for spin-down states. The $W_{0.25}V_{0.75}Se_2$ alloy can be used as a spin filter tunneling barrier exploiting this fascinating property. High spin polarization of the tunnel current was found for the alloy. Furthermore, under the Curie temperature, electrical conductivity for the spin-up channel was found to be zero, while conductivity for the spin-down channel was around 10^{19} $(\Omega\ cm\ s)^{-1}$ when the chemical potential was 0.2 eV greater than the Fermi energy. Changes in optical properties were also investigated through time-dependent density functional theory calculations. The findings of this study will be beneficial for proposing new magnetic monolayer alloys for application in nanoscale spintronic devices.

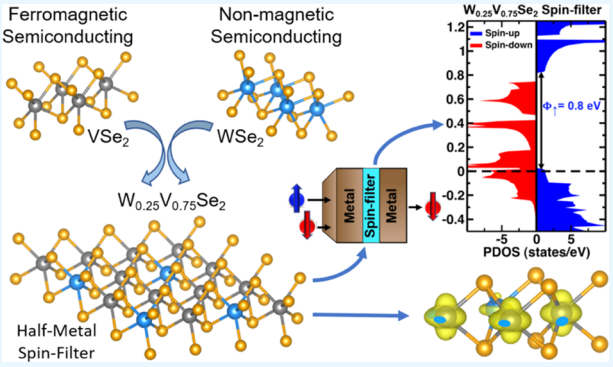

1. INTRODUCTION

Transition metal dichalcogenides (TMDs) have recently garnered much attention among the scientific community due to their intriguing physical, chemical, electronic, and optical properties. Much of the research have been focused on monolayer TMDs constructed from group 6 (VIB) materials, such as WS_2, WSe_2, MoS_2, and $MoSe_2$. They are direct band gap semiconductors with excellent electronic and optical properties, which make them viable candidates for electronic,[1] photonic,[2] optoelectronic,[3,4] and valleytronic devices.[5] However, in most cases, defect-free pristine TMDs are nonmagnetic because there are no unsaturated bonds and no magnetic elements. This nonmagnetic nature prevents their spintronic applications.

During the growth process edges, dislocations, grain boundaries, and other imperfections may occur which alter the electronic and magnetic properties of the TMDs. Chalcogen vacancies in WSe_2 monolayers introduced changes in electronic properties, such as band gap narrowing and increase of electron−hole effective masses.[6] Moreover, it was reported that induced magnetism in defected monolayer WSe_2 was found as a result of two W atom vacancies.[7] Structural defects such as vacancies are intrinsically generated in as grown WSe_2 monolayers.[8] However, achieving proper growth control of magnetism inducing defects in TMDs through structural engineering methods can be very difficult.

Although VSe_2 exists only in the T phase in nature, T to R polytype transformation have been observed through Cu deposition in thin VSe_2 surface layers or by intercalating Cu into bulk VSe_2.[9] H-type single layer components were found in the R polytype VSe_2 bulk as the only difference between H-WSe_2 and R-VSe_2 is the stacking patterns of sandwich layers. From first-principles calculation, monolayer 1H-VSe_2 was found to be a ferromagnetic (FM) semiconducting material,[10] whereas monolayer WSe_2 is a nonmagnetic semiconductor with a direct band gap.[6] Previously, there have been reports of vanadium-doped WSe_2 behaving as dilute magnetic semiconductors.[11,12] However, doping TMDs may suffer from several disadvantages, such as alteration of the lattice structure, formation of defects or dislocations, and reduced mobility due to different scattering mechanisms. In contrary, growth of highly pure crystals of $W_{0.75}V_{0.25}Se_2$ and $W_{0.25}V_{0.75}Se_2$ alloy was demonstrated through the direct vapor transport technique.[13,14] These alloys showed excitonic resonances and fast rise and decay of photo current, efficient absorption for photodetection applications. However, the possibility of creating monolayer FM semiconducting

Received: May 27, 2022
Accepted: September 26, 2022
Published: October 6, 2022

material through tungsten vanadium selenide alloys has yet to be explored.

In this work, we explored the possibility of inducing magnetism in monolayer WSe_2 by alloying it with VSe_2 using first-principles calculations. By alloying in different compositions, interesting changes can be found in electronic and magnetic properties from their pristine crystals. To comprehend how the lattice structure changes with alloying, we reported the optimized ground state structure found through density functional theory (DFT) calculations. Electronic and magnetic properties such as spin-polarized E-k diagram with and without spin−orbit coupling (SOC), orbital projected band diagram (fatbands), projected density of states (PDOS), charge density difference, Bader charge transfer, total magnetism, and magnetism distributions were analyzed for different alloy compositions. Our investigation of inducing long-range magnetic order in 2D TMDs through alloying can be vital for future spintronic devices. Additionally, spin-polarized splitting of conduction bands were studied. Ferromagnetic semiconductors showing exchange splitting of conduction bands in the magnetically ordered state can be used as spin filter tunneling barriers[15] in spin filter transistors.[16] To investigate the spin-filtering capability of $W_{1-x}V_xSe_2$ alloys, spin polarization of tunnel current and temperature-dependent spin-polarized electrical conductivity was calculated. Additionally, we studied optical properties by utilizing time-dependent DFT calculations. Exciting electronic, magnetic and optical properties revealed from our study uphold the potential of these alloys in emerging applications.

2. COMPUTATIONAL DETAILS

The electronic and magnetic properties of the monolayers were calculated using Quantum ESPRESSO[17,18] which is based on DFT. Projector augmented wave (PAW) pseudopotentials of tungsten, vanadium, and selenium were used with exchange−correlation functional described by the Perdew−Burke−Ernzerhof (PBE) functional within the generalized-gradient approximation (GGA). Marzari-Vanderbilt-DeVita-Payne cold smearing[19] of 0.01 Ry was used to describe the electron occupations. Kinetic energy cutoff of 50 Ry was used for electron wave functions and kinetic energy cutoff of 500 Ry was used for charge density and potential. Structural relaxation were performed until forces on atoms converged down to 10^{-3} Ry/Bohr and minimum difference in total energies were less than 10^{-8} Ry. A $(8 \times 8 \times 1)$ Γ-centered Monkhorst−Pack grid was used for spin-polarized self-consistent field calculations. Non-self-consistent field calculations were performed using a $(32 \times 32 \times 1)$ *k*-point grid to get the density of states (DOS). E-k diagrams were computed along the Γ−M−K−Γ path of the first Brillouin zone and 20 *k*-points were calculated between each high symmetry points. To observe the effect of SOC, band diagrams for pristine WSe_2, VSe_2, and alloy monolayers were also calculated using fully relativistic PAW pseudopotentials of W, V, and Se atoms with the GGA-PBE exchange−correlation functional.

A $(2 \times 2 \times 1)$ supercell of monolayer WSe_2 with hexagonal symmetry was created using lattice parameters which matches with experimentally determined crystal structure.[20] A vacuum region of 15 Å was added along the *z*-axis to avoid van der Waals interaction between the periodic images of the monolayers. Pure VSe_2 (V_4Se_8 supercell) and the subsequent alloys—$W_{0.75}V_{0.25}Se_2$ (W_3VSe_8 supercell), $W_{0.5}V_{0.5}Se_2$ ($W_2V_2Se_8$ supercell), and $W_{0.25}V_{0.75}Se_2$ (WV_3Se_8 supercell)—were created from the $(2 \times 2 \times 1)$ supercell of 1H-WSe_2 (W_4Se_8 supercell) monolayer by replacing W atom(s) with V atom(s). All the crystal structures were optimized using variable cell relaxation but allowing only x and y components of the cell to change, thus constraining the vacuum region along the *z*-axis.

The projection of W, V, and Se atomic orbitals on the band dispersion and density of states were determined using Quantum ESPRESSO simulation package. Bader charge analysis for charge distributions in the atoms was conducted using the code developed by the Henkelman group.[21] Furthermore, temperature-dependent electrical conductivity was calculated using the BoltzTraP code[22] within the limitations of the Boltzmann theory and constant relaxation time approximation (see the Supporting Information for details). The calculations were performed on top of the ground state DFT calculation from Quantum ESPRESSO using a dense $(32 \times 32 \times 1)$ *k*-point grid.

Ground state electronic structure calculations for the optical properties were done in Quantum ESPRESSO using norm-conserving pseudopotentials with PBE exchange−correlation functional. Optical properties were calculated by solving the Dyson equation[23] within the time-dependent DFT formalism as implemented in the YAMBO code.[24] After convergence testing, response block size of the dielectric matrix was taken as 3 Ry. The energy cutoff for expanding the wave functions was taken as 3 Ry. A total of 40 bands were taken for summing over the states in the random phase approximation response function. From the calculated complex dielectric constant, we obtained complex refractive index spectra which were used to calculate reflectance, transmittance, and absorption coefficient of all the monolayers (see the Supporting Information for details).

3. RESULTS AND DISCUSSION

Pristine WSe_2, VSe_2, and their derivative alloys ($W_{0.75}V_{0.25}Se_2$, $W_{0.5}V_{0.5}Se_2$, and $W_{0.25}V_{0.75}Se_2$) were optimized and their lattice constants, bond lengths, and bond angles were thoroughly investigated to determine the effect of alloying on the structural properties (see Table 1). Pristine VSe_2 and the monolayer alloys were found to be dynamically stable as can be seen from Figure S1 of the Supporting Information. Pristine structures along with structures with different compositions of V and W are illustrated in Figure 1a−f.

Table 1. Effect of Alloying on the Structural Parameters

	lattice constant	bond length (Å)		bond angle	
crystal structures	a = b (Å)	W-Se	V-Se	∠Se-W-Se	∠Se-V-Se
WSe_2 (W_4Se_8)	6.638	2.547		82.39°	
$W_{0.75}V_{0.25}Se_2$ (W_3VSe_8)	6.649	2.542	2.506	80.83°	82.26°
		2.549		82.32°	
$W_{0.5}V_{0.5}Se_2$ ($W_2V_2Se_8$)	6.677	2.533	2.542	79.94°	79.95°
		2.542	2.499	80.69°	82.04°
$W_{0.25}V_{0.75}Se_2$ (WV_3Se_8)	6.661	2.537	2.501	79.78°	79.98°
			2.512		80.71°
VSe_2 (V_4Se_8)	6.688		2.508		79.32°

As the composition of the V atom was increased, lattice constant also increased. Bond length between the V and Se atom was generally smaller than bond length between W and Se atoms in the crystal structures. This was due to the fact that V had one less valence electron in the d subshell than W. In the $W_{0.75}V_{0.25}Se_2$ alloy, the W-Se bond length was larger when the Se atom was shared only with W atoms and became smaller when Se was shared with a V atom. The same trend was observed

https://doi.org/10.1021/acsomega.2c03312
ACS Omega 2022, 7, 36184−36194

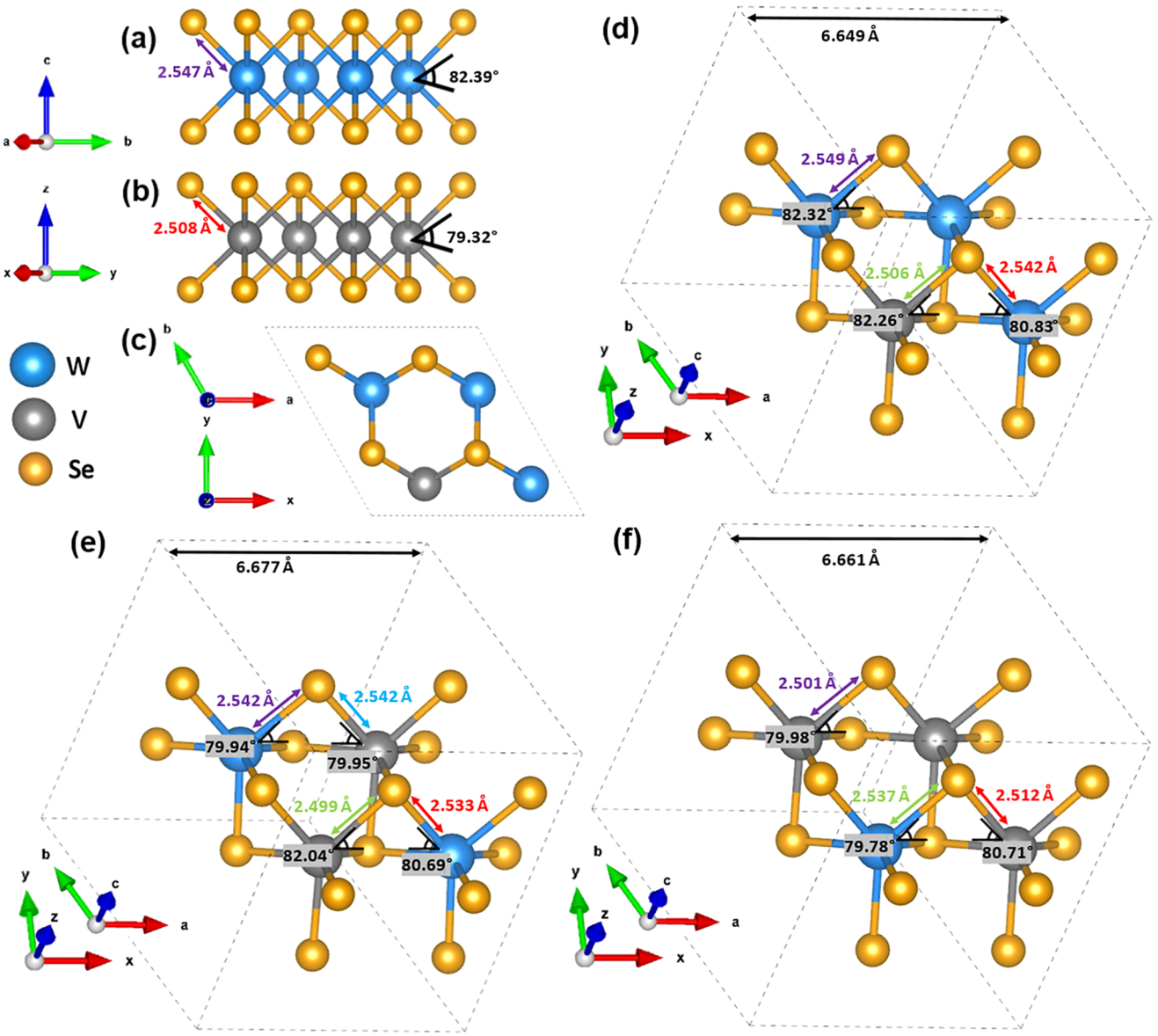

Figure 1. Optimized structures of different monolayers: (a) pristine WSe_2 (W_4Se_8 supercell), (b) pristine VSe_2 (V_4Se_8 supercell), (c,d) $W_{0.75}V_{0.25}Se_2$ alloy (W_3VSe_8 supercell), (e) $W_{0.5}V_{0.5}Se_2$ alloy ($W_2V_2Se_8$ supercell), and (f) $W_{0.25}V_{0.75}Se_2$ alloy (WV_3Se_8 supercell). Lattice constants, bond lengths, and bond angles are illustrated here.

Table 2. Formation Energy of $W_{1-x}V_xSe_2$ Alloy Monolayers

crystal structures	formation energy (eV)
$W_{0.75}V_{0.25}Se_2$	0.0494
$W_{0.5}V_{0.5}Se_2$	0.0847
$W_{0.25}V_{0.75}Se_2$	0.0812

in the $W_{0.5}V_{0.5}Se_2$ alloy where the W-Se bond length decreased further when the Se atom was shared only with V atoms. The angle created by Se, W, and Se atoms, ∠Se-W-Se, in the pristine WSe_2 monolayer was found to be 82.39°. For the case of pristine VSe_2 monolayer, ∠Se-V-Se was 79.32°. Both ∠Se-W-Se and ∠Se-V-Se angles in the alloys were smaller than ∠Se-W-Se of pure WSe_2. This deviation arose from the addition of V atoms. The upper and lower Se layers tended to move toward the transition metal layer when V atoms were added. Hence, the lattice constant was larger in the alloys compared to WSe_2.

To determine the energetic stability of the considered systems, formation energy was calculated using total energy of $(2 \times 2 \times 1)$ supercells of pristine and alloy monolayers computed from DFT study. Formation energy for the alloy monolayers were determined using the equation

$$E_{\text{formation}} = E_{W_{1-x}V_xSe_2} - (1-x) \times E_{WSe_2} - x \times E_{VSe_2} \quad (1)$$

Here, $E_{\text{formation}}$ is the formation energy of the alloys, $E_{W_{1-x}V_xSe_2}$ represents total energy of alloy monolayer, where $x = 0.25$, 0.5, and 0.75. E_{WSe_2} and E_{VSe_2} are total energies of pristine WSe_2 and VSe_2 monolayers, respectively. Calculated formation energies are shown in Table 2.

Formation energy for all the alloys was positive and had a very small value less than 0.1 eV. As the formation energy is positive, external factors such as temperature or pressure will be required to form the alloy monolayers from pristine monolayers. Among the alloys, $W_{0.75}V_{0.25}Se_2$ had the lowest formation energy and the formation energy was higher for higher vanadium compositions.

https://doi.org/10.1021/acsomega.2c03312
ACS Omega 2022, 7, 36184−36194

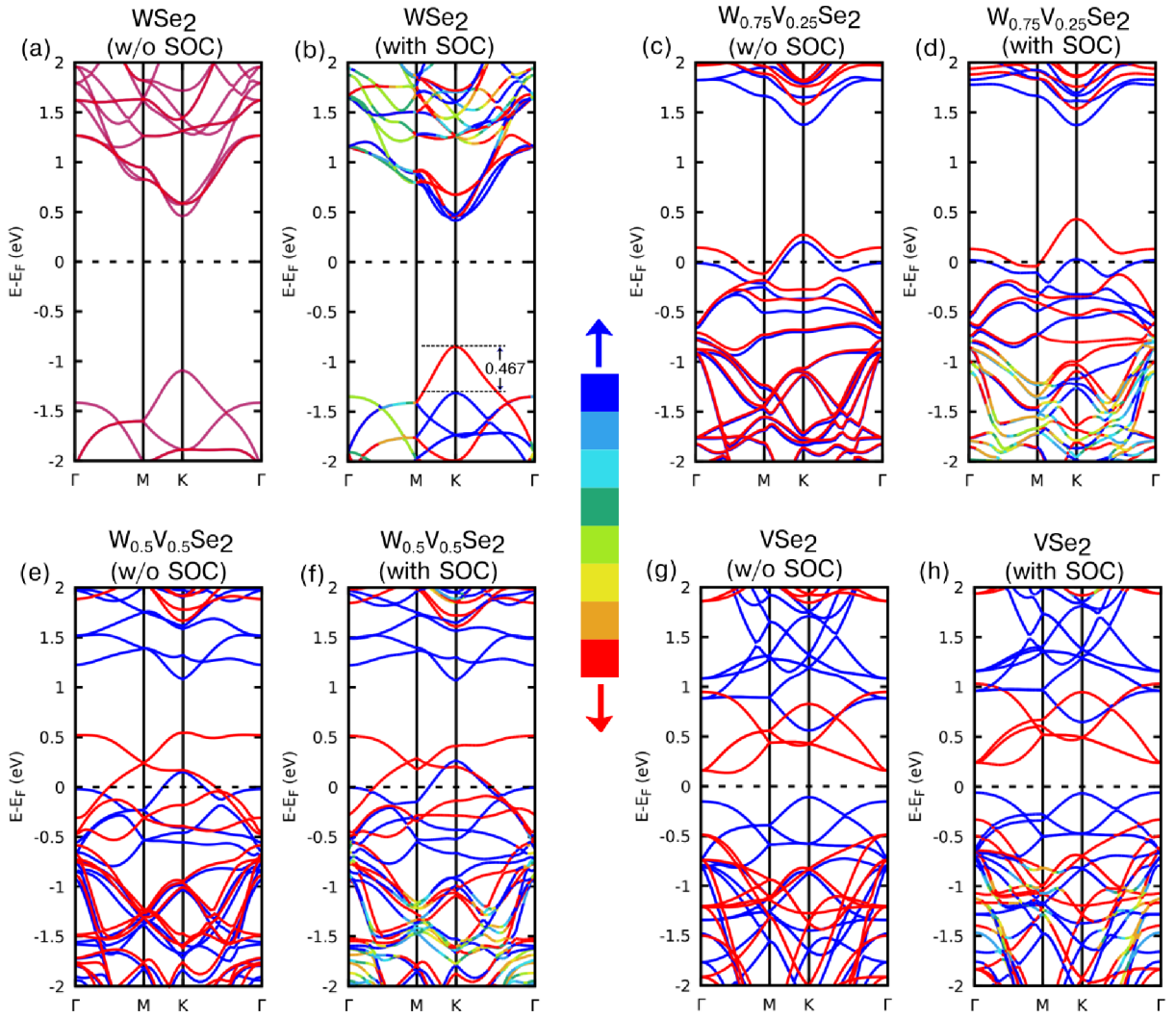

Figure 2. Spin-polarized band diagram without SOC for different monolayers: (a) WSe_2 (W_4Se_8 supercell), (c) $W_{0.75}V_{0.25}Se_2$ (W_3VSe_8 supercell), (e) $W_{0.5}V_{0.5}Se_2$ ($W_2V_2Se_8$ supercell), and (g) VSe_2 (V_4Se_8 supercell). Spin-up and spin-down bands are represented by blue and red lines, respectively. Band diagram including SOC for (b) WSe_2, (d) $W_{0.75}V_{0.25}Se_2$, (f) $W_{0.5}V_{0.5}Se_2$, and (h) VSe_2. The color gradient from blue to red represents expectation values of the spin operator along [001] direction ranging from +1/2 to −1/2.

The formation energy is comparable to other monolayer TMD alloys such as $Mo_{1-x}V_xS_2$ and $Mo_{1-x}Cr_xS_2$.[25]

Spin-polarized band diagram with and without including SOC for WSe_2, $W_{0.75}V_{0.25}Se_2$ (W_3VSe_8 supercell), $W_{0.5}V_{0.5}Se_2$ ($W_2V_2Se_8$ supercell), and VSe_2 monolayers are shown in Figure 2. Without SOC, the pristine WSe_2 monolayer was found as a semiconductor with a direct band gap of 1.55 eV which matched well with previous reports.[6,7] Spin-up and spin-down bands were degenerate resulting in zero magnetic moment for this structure. With SOC, a large splitting of 0.467 eV was found at the valence band maximum (VBM) between spin-down and spin-up states in WSe_2. This is consistent with previous report.[26] Splitting was also noticeable in the conduction band minimum (CBM). However, the amount of splitting was much smaller compared to VBM. The direct band gap after including SOC was found to be 1.26 eV (compared to 1.55 eV without SOC) which is consistent with previously reported value.[27] In the case of the pristine 1H-VSe_2 monolayer, an indirect band gap of 0.234 eV was observed without SOC, which is consistent with the previous report .[28] To find the most stable magnetic order, total energies for both FM and anti-FM (AFM) cases were computed for VSe_2 using a (4 × 4 × 1) supercell. Total energy for FM case was less than total energy for the AFM case (see the Supporting Information). Hence, it can be concluded that monolayer VSe_2 is a FM semiconducting material. Total magnetization of the V_4Se_8 supercell was 4.00 μ_B. VBM occurred at K point originating from a spin-up state and CBM occurred between Γ and K points originating from a spin-down state. After including SOC, two spin-up bands and two spin-down bands below the Fermi level underwent a small amount of splitting along the Γ−M path. Similarly, two spin-down bands above the Fermi level showed splitting along the same k-path. Expectation value of the spin operator along [001] direction was maximum (spin-up, +1/2) or minimum (spin-down, −1/2) around the Fermi level as can be seen from Figure 2h where blue and red lines represent spin-up and spin-down bands, respectively. Separation in spin-up states and spin-down states confirms the presence of magnetic moment after including SOC. Total magnetization was similar to without SOC case, which is evident from the similar positions of spin-up and spin-down bands in both cases.

To find the ground state magnetic ordering of the alloys, both FM and AFM magnetic configurations were considered using (4 × 4 × 1) supercells of monolayer alloys. Total energy for FM configurations was found to be lower than AFM configurations

https://doi.org/10.1021/acsomega.2c03312
ACS Omega 2022, 7, 36184−36194

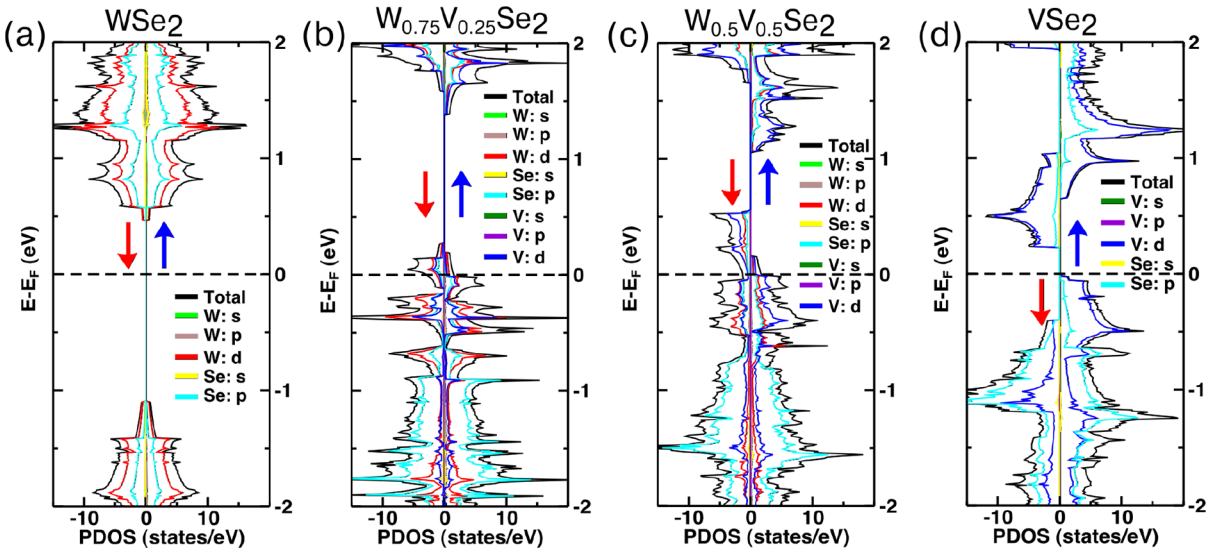

Figure 3. PDOS without including SOC for different monolayers: (a) WSe_2 (W_4Se_8 supercell), (b) $W_{0.75}V_{0.25}Se_2$ (W_3VSe_8 supercell), (c) $W_{0.5}V_{0.5}Se_2$ ($W_2V_2Se_8$ supercell), and (d) VSe_2 (V_4Se_8 supercell). Spin-up and spin-down components of the PDOS are marked by blue and red arrows, respectively.

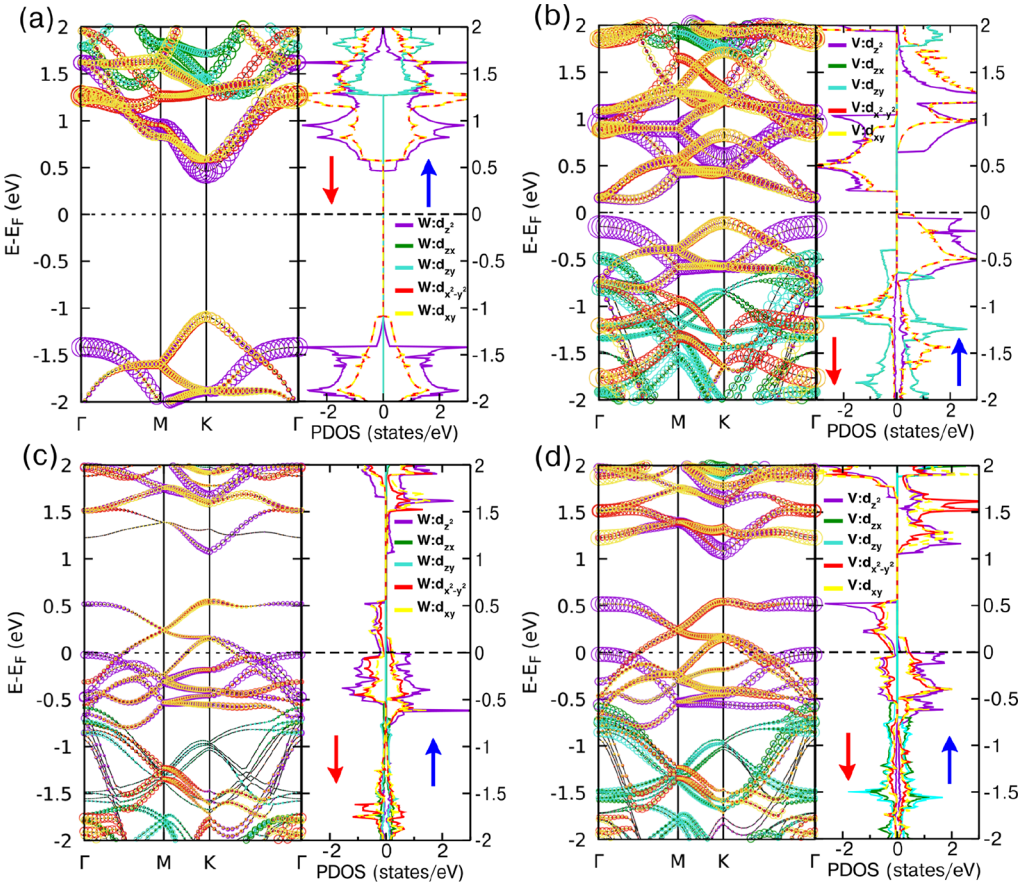

Figure 4. Orbital projected E-k diagrams and PDOS without SOC for (a) WSe_2 (W_4Se_8 supercell), (b) VSe_2 (V_4Se_8 supercell), and (c,d) $W_{0.5}V_{0.5}Se_2$ ($W_2V_2Se_8$ supercell). Spin-up and spin-down bands are grouped together in the E-k diagrams. In the E-k diagrams, size of the circles indicate amount of contribution. Only d orbitals of W and V atoms are shown as they have the most significant contributions around the Fermi level. Spin-up and spin-down components of the PDOS are marked by blue and red arrows, respectively.

(see the Supporting Information for details). Our calculation showed that magnetic moment contribution from each V atom of any particular monolayer was identical for various sizes of supercells. Hence, all the alloys demonstrated long-range FM order with different total magnetization. For $W_{0.75}V_{0.25}Se_2$, Fermi level shifted inside the valence band. This suggests that this alloy will show a metallic behavior. A total magnetization of 0.38 μ_B/cell was observed for this structure. As the

https://doi.org/10.1021/acsomega.2c03312
ACS Omega 2022, 7, 36184−36194

Table 3. Magnetization Induced in $W_{1-x}V_xSe_2$ Monolayers

crystal structures	total magnetization (per cell)
WSe_2(W_4Se_8 supercell)	0.0 μ_B
$W_{0.75}V_{0.25}Se_2$(W_3VSe_8 supercell)	0.38 μ_B
$W_{0.5}V_{0.5}Se_2$($W_2V_2Se_8$ supercell)	1.53 μ_B
$W_{0.25}V_{0.75}Se_2$(WV_3Se_8 supercell)	2.97 μ_B
VSe_2(V_4Se_8 supercell)	4.00 μ_B

concentration of V was increased in $W_{0.5}V_{0.5}Se_2$, total magnetization increased to 1.53 μ_B/cell. Fermi level moved further into the valence band. Atomic orbital projected DOS without SOC for pristine WSe_2, VSe_2, and the alloys are presented in Figure 3. PDOS of WSe_2 indicated that d orbitals of W atoms contributed significantly in the bands near Fermi level as can be seen in Figure 3a. Similarly, for VSe_2, states around the Fermi level mostly originated from d orbitals of V atoms. For $W_{0.75}V_{0.25}Se_2$ and $W_{0.5}V_{0.5}Se_2$ alloy, states around CBM and VBM were found to be originating from both W-d and V-d orbitals. Though difference in DOS originating from W-d orbitals and V-d orbitals was not much in $W_{0.75}V_{0.25}Se_2$, for $W_{0.5}V_{0.5}Se_2$, a stark increase of V-d orbital states was seen, especially around the CBM. Specific d orbital contributions were investigated in detail and elaborated later (see Figure 4). Similar kind of trend could be seen in case of $W_{0.25}V_{0.75}Se_2$ alloy. For this alloy, an increased total magnetization of 2.97 μ_B/cell was observed. Spin-up and spin-down bands became further separated. The magnetization originated from V atoms and as the percentage of V atom was increased in the alloys, total magnetization also increased. Total magnetization found in the monolayers is summarized in Table 3. Positions of spin-up and spin-down bands in the monolayer alloys after including SOC were similar to their without SOC cases, resulting in similar total magnetization with and without SOC. However, splitting between the spin-up and spin-down bands changed. In the case of $W_{0.75}V_{0.25}Se_2$, energy difference between the two spin-up and spin-down bands above the Fermi level at K point increased from 0.07 eV (without SOC) to 0.4 eV (with SOC), as can be seen from Figure 2c,d. The spin-up band shifted down toward the Fermi level, while the spin-down band shifted upward. This characteristic is similar to splitting of VBM in pristine WSe_2. This was expected as both spin-up and spin-down states above the Fermi level at K point in $W_{0.75}V_{0.25}Se_2$ originated mostly from $d_{x^2-y^2}$ (26.7%) and d_{xy} (26.7%) orbitals of W atoms (see Table 4 and Figure S3 of the Supporting Information). In the case of $W_{0.5}V_{0.5}Se_2$ and $W_{0.25}V_{0.75}Se_2$ (see the Supporting Information for band diagram of $W_{0.25}V_{0.75}Se_2$ with SOC), splitting of bands after including SOC was mostly observed along the Γ−M path similar to pristine VSe_2. This can be attributed to the fact that d orbitals of V atoms contributed more than d orbitals of W atoms around the Fermi level in these alloys. As the overall band structures of pristine VSe_2, WSe_2, and the alloys were similar for with SOC and without SOC cases, orbital projection of band structure and DOS were performed for the without SOC case, which is enough to give a detailed description of the electronic properties.

For detailed analysis of the electronic properties, projection of atomic orbitals was performed on the band structure and DOS. The d orbitals of W and V atoms predominantly contributed to the bands near the Fermi level. Figure 4a−d shows their contributions for the different crystal structures. Contributions from the other orbitals are provided in the Supporting Information. For WSe_2, VBM consisted primarily of $d_{x^2-y^2}$ (37.6%) and d_{xy} (37.6%) orbitals of W atoms. Other orbital contributions came from p_x (10.4%), p_y (10.4%) orbitals of Se atoms and p_x (1.2%), p_y (1.2%) orbitals of W atoms. On the other hand, CBM consisted primarily of d_{z^2} (81.2%) orbitals of W atoms. Rest of the contribution came from s (11.2%) orbitals of W atoms and p_x (3.2%) and p_y (3.2%) orbitals of Se atoms. For VSe_2, VBM consisted primarily of $d_{x^2-y^2}$ (44.0%) and d_{xy} (44.0%) orbitals of V atoms. Other orbital contributions came from p_x (5.6%), p_y (5.6%) orbitals of Se atoms. Unlike WSe_2, CBM of VSe_2 occurred in between the Γ and K point. It consisted primarily of d_{z^2} (35.2%), and d_{xy} (32.4%) orbitals of V atoms. Rest of the contribution came from $d_{x^2-y^2}$ (10.8%) of V atoms, p_z (10.4%) orbitals of Se atoms, s (2.4%) orbitals of V atoms, and p_x (1.6%) orbitals of Se atoms.

As majority of the contribution at VBM and CBM came from d orbitals of W and V atoms, their projection on the bands is shown for the $W_{0.5}V_{0.5}Se_2$ alloy in Figure 4c,d. Fermi level rested inside the valence band. Due to the upward shift of valence bands, there were one empty spin-up and two empty spin-down states in the K direction. The VBM and CBM both occurred at K point with a gap of 0.539 eV. In VBM, $d_{x^2-y^2}$ and d_{xy} orbitals of V atoms contributed a total of 45.0%. On the other hand, $d_{x^2-y^2}$ and d_{xy} orbitals of W atoms contributed a total of 35.6%. In CBM, d_{z^2} orbital of V atoms contributed 56.4%, whereas d_{z^2} orbitals of W atoms contributed 21.0%. This clearly shows that d orbitals of V atoms have more dominant presence in valence and conduction band edges than the W atoms. This trend was also seen in the other compositions of the $W_{1-x}V_xSe_2$ alloy. Table 4 summarizes the orbital contributions at VBM and CBM of different alloy compositions. Orbital projected DOS for d orbitals of W and V atoms of $W_{0.5}V_{0.5}Se_2$ ($W_2V_2Se_8$ supercell) alloy is shown in Figure 4c,d. Spin-up and spin-down DOS diagrams were found to be asymmetrical for d orbitals of both W and V atoms. The asymmetry was higher for the case of d orbitals of V atoms. Spin-up and spin-down states above the Fermi level and around the band edges were dominated by d orbitals of V atoms.

Spin-polarized E-k diagram along with PDOS of W, V, and Se atoms of $W_{0.25}V_{0.75}Se_2$ (WV_3Se_8 supercell) is shown in Figure 5a. There was a direct band gap of 0.8 eV between spin-up states in the conduction and valence band, while there was no gap between occupied and unoccupied spin-down states. This opens

Table 4. d Orbital Contributions of W and V Atoms in the Pristine Crystals and Their Alloys

monolayer	contribution at VBM				contribution at CBM			
	W-$d_{x^2-y^2}$	W-d_{xy}	V-$d_{x^2-y^2}$	V-d_{xy}	W-d_{z^2}	V-d_{z^2}	V-$d_{x^2-y^2}$	V-d_{xy}
WSe_2	37.6%	37.6%			81.2%			
$W_{0.75}V_{0.25}Se_2$	26.7%	26.7%	12.3%	12.3%	31.5%	44.3%		
$W_{0.5}V_{0.5}Se_2$	13.6%	22.0%	27.2%	17.8%	21.0%	56.4%		
$W_{0.25}V_{0.75}Se_2$	6.3%	6.3%	36.8%	36.7%	9.7%	74.7%		
VSe_2			44.0%	44.0%		35.2%	32.4%	10.8%

https://doi.org/10.1021/acsomega.2c03312
ACS Omega 2022, 7, 36184−36194

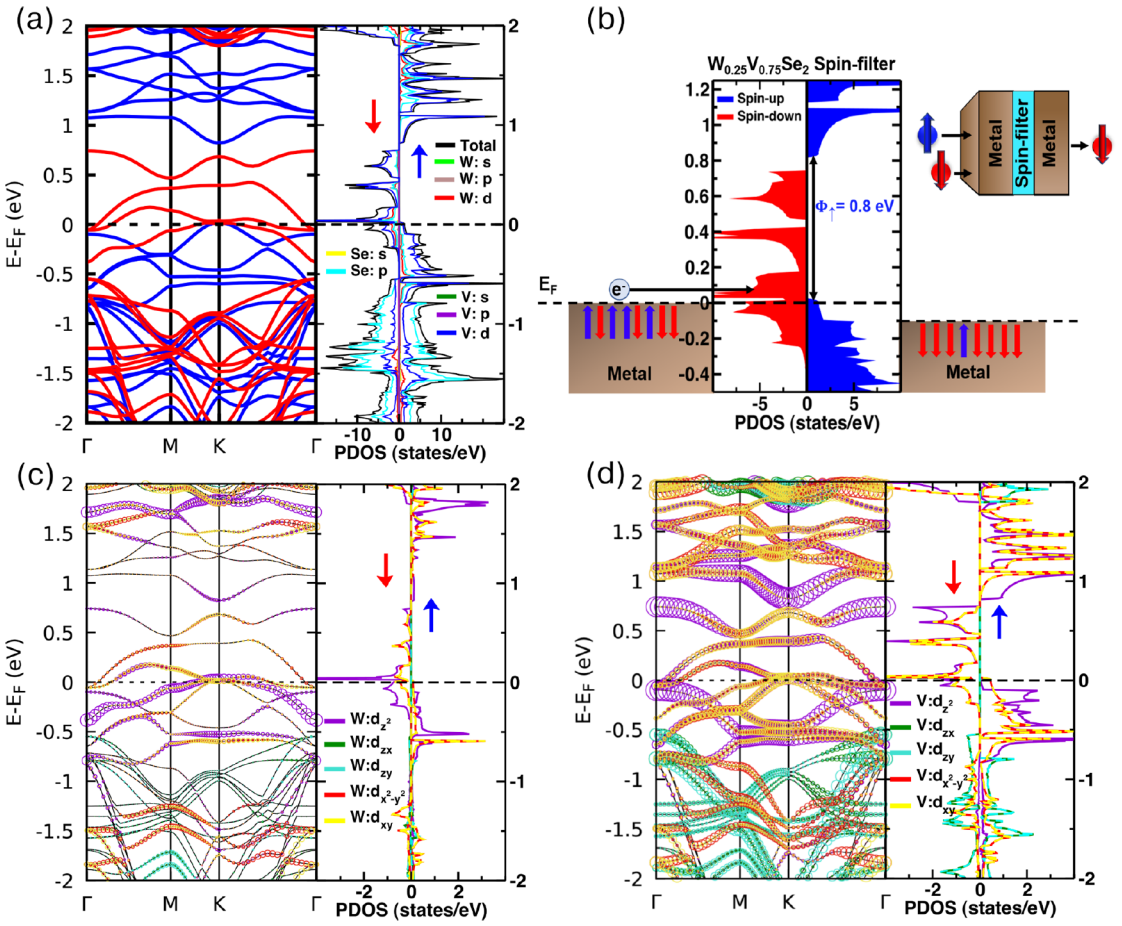

Figure 5. (a) Spin-polarized E-k diagram and PDOS without SOC for the $W_{0.25}V_{0.75}Se_2$ (WV_3Se_8 supercell) alloy. (b) Schematic arrangement of $W_{0.25}V_{0.75}Se_2$ as a spin-filter tunneling barrier between two metal electrodes. (c,d) Projection of d orbitals of W and V atoms on the band diagram and DOS without SOC for the $W_{0.25}V_{0.75}Se_2$ alloy. In the E-k diagrams, size of the circles signify the amount of contribution.

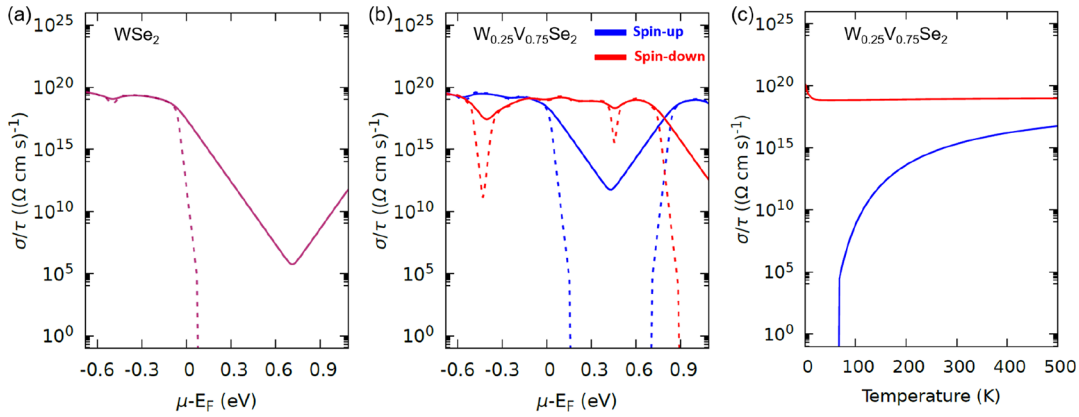

Figure 6. Electrical conductivity relative to relaxation time (σ/τ) plotted as a function of chemical potential (μ-E_F) for the spin-up channel (blue curve) and spin-down channel (red curve) for (a) WSe_2 and (b) $W_{0.25}V_{0.75}Se_2$. Dashed curve represents conductivity at 50 K temperature, while solid curve represents conductivity at 300 K temperature. (c) Change in conductivity with respect to temperature for $W_{0.25}V_{0.75}Se_2$ at μ-E_F = 0.2 eV.

up the opportunity to use $W_{0.25}V_{0.75}Se_2$ as a spin-filter tunneling barrier. During the tunneling process, spin is conserved. Spin-down electrons should not face any barrier during tunneling because of available unoccupied states. However, spin-up electrons see a barrier of 0.8 eV during tunneling. This could give rise to a highly spin-polarized current filtering out spin-up electrons using spin filter effect. This effect is shown schematically in Figure 5b. From the PDOS, it was evident that spin-down states between the band gap of spin-up states mostly came from d orbitals of V atoms. Figure 5c,d shows contributions of d orbitals of W and V atoms. V-d_{z^2}, V-d_{xy}, and V-$d_{x^2-y^2}$ orbitals mostly contributed to the spin-down states located between the mid gap of spin-up CBM and VBM states.

In the metal/$W_{0.25}V_{0.75}Se_2$/metal structure shown in Figure 5b, when electrons with random spin polarization tunnel from the left metal through the $W_{0.25}V_{0.75}Se_2$ spin-filter, spin-up electrons get filtered out because of the gap present in spin-up channel. On the other hand, spin-down electrons can tunnel

https://doi.org/10.1021/acsomega.2c03312
ACS Omega 2022, 7, 36184−36194

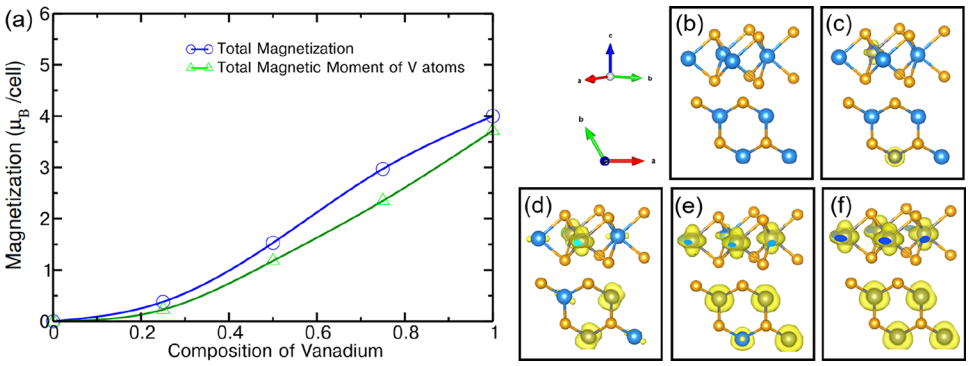

Figure 7. (a) Total magnetization and total atomic magnetic moment of V atoms in $W_{1-x}V_xSe_2$ monolayers as a function of V atom composition. Magnetism distribution of (b) pristine WSe_2 (W_4Se_8 supercell), (c) $W_{0.75}V_{0.25}Se_2$ (W_3VSe_8 supercell) alloy, (d) $W_{0.5}V_{0.5}Se_2$ ($W_2V_2Se_8$ supercell) alloy, (e) $W_{0.25}V_{0.75}Se_2$ (WV_3Se_8 supercell) alloy, and (f) pristine VSe_2 (V_4Se_8 supercell). Isosurface value was set to be 0.008 e/Bohr^3.

Table 5. Average Charge Transfer from Bader Charge Analysis

crystal structures	average charge transfer		
	V	Se	W
WSe_2(W_4Se_8 supercell)		−0.50947375	+1.01902675
$W_{0.75}V_{0.25}Se_2$ (W_3VSe_8 supercell)	+1.180299	−0.53572675	+1.035342
$W_{0.5}V_{0.5}Se_2$ ($W_2V_2Se_8$ supercell)	+1.184901	−0.565672	+1.0774385
$W_{0.25}V_{0.75}Se_2$ (WV_3Se_8 supercell)	+1.180041	−0.574831375	+1.058224
VSe_2(V_4Se_8 supercell)	+1.19390175	−0.59698425	

through the filter easily and a highly spin-polarized current with a large number of spin-down electrons is found in the right metal electrode. The barrier height for spin-up states, $\Phi_\uparrow$, was found to be 0.8 eV, while the barrier height for the spin-down state, $\Phi_\downarrow$, was 0 eV. For a fixed barrier thickness, spin-up tunnel current density, $J_\uparrow$, and spin-down tunnel current density, $J_\downarrow$, depend exponentially on the corresponding $\Phi_{\uparrow(\downarrow)}$ as the relation given by[29]

$$J_{\uparrow(\downarrow)} \propto \exp(-\Phi_{\uparrow(\downarrow)}^{1/2}) \tag{2}$$

Here, the exchange splitting, which is difference in barrier heights of spin-up and spin-down electrons, was $\Phi_\uparrow - \Phi_\downarrow = 0.8$ eV. This resulted in a very high spin polarization of the tunnel current, $P = 42\%$ obtained from the equation

$$P = \frac{J_\uparrow - J_\downarrow}{J_\uparrow + J_\downarrow} \tag{3}$$

EuO, EuS, and EuSe were reported to exhibit spin filtering behavior with less exchange splittings.[15,30,31] In these materials, spin-up electrons had lower barrier height than spin-down electrons. Therefore, in contrast to $W_{0.25}V_{0.75}Se_2$, spin-down electrons would be filtered out instead of spin-up electrons in these materials.

The condition of spin-filtering was still present after including SOC in $W_{0.25}V_{0.75}Se_2$. The band diagram of $W_{0.25}V_{0.75}Se_2$ with SOC is shown in the Supporting Information. After incorporating SOC, two spin-down bands touching each other at K point just above the Fermi level underwent a splitting of 0.11 eV. The VBM for spin-up state shifted slightly downward increasing the barrier height for spin-up channel from 0.80 eV (without SOC) to 0.88 eV (with SOC). This resulted in an increase in spin-polarization of tunnel current from 42% (without SOC) to 44% (with SOC).

Curie temperature, T_C, can be obtained using the mean field expression[32]

$$T_C = \frac{2(E_{AFM} - E_{FM})}{3k_B N} \tag{4}$$

Here, N is the number of magnetic ions in the magnetic unit cell, k_B is the Boltzmann constant, E_{AFM} is the total energy in AFM state, and E_{FM} is the total energy in the FM state. T_C of $W_{0.25}V_{0.75}Se_2$ was estimated to be 59.57 K. The magnetic configurations and total energies are provided in the Supporting Information.

Electrical conductivity relative to relaxation time, σ/τ with respect to chemical potential for WSe_2 and $W_{0.25}V_{0.75}Se_2$ is shown in Figure 6a,b for 50 and 300 K temperature. Details about how the electrical conductivity was calculated are mentioned in the Supporting Information. As WSe_2 was found to be a non-magnetic direct band gap semiconductor, σ/τ for spin-up channel overlapped spin-down channel. σ/τ for both channels dropped sharply above the Fermi energy due to the presence of the band gap. For $W_{0.25}V_{0.75}Se_2$, σ/τ for spin-up channel showed distinct behavior compared to the spin-down channel. When the chemical potential was increased above the Fermi energy, electrical conductivity for spin-up channels dropped sharply and became zero at 0.16 eV for 50 K temperature. However, conductivity for the spin-down channel was around the order of 10^{19} $(\Omega\ \text{cm}\ \text{s})^{-1}$ when chemical potential was above the Fermi energy. Similarly, conductivity for the spin-up channel in $W_{0.25}V_{0.75}Se_2$ dropped sharply above the Fermi energy by an order of 7 in magnitude compared to spin-down channel at 300 K. The spin-up channel introduced a barrier acting as a semiconductor, while the spin-down channel showed metallic characteristics. At 0.43 eV, σ/τ for the spin-up channel was 5.86×10^{11} $(\Omega\ \text{cm}\ \text{s})^{-1}$, while σ/τ for the spin-down channel was 2.77×10^{18} $(\Omega\ \text{cm}\ \text{s})^{-1}$. Thus, the spin-down channel number was significantly greater compared to the spin-up channel number, and consequently, the spin-down channel had a huge conductance. Figure 6c shows the change in spin-up and spin-down conductivity with temperature at a certain chemical potential ($\mu - E_F = 0.2$ eV). Conductivity for the spin-up channel was zero until 60 K and afterward, it started rising with the increase in temperature. Interestingly, spin-up conductivity was always lower than spin-down conductivity which make this alloy particularly functional for spintronic devices.

https://doi.org/10.1021/acsomega.2c03312
ACS Omega 2022, 7, 36184−36194

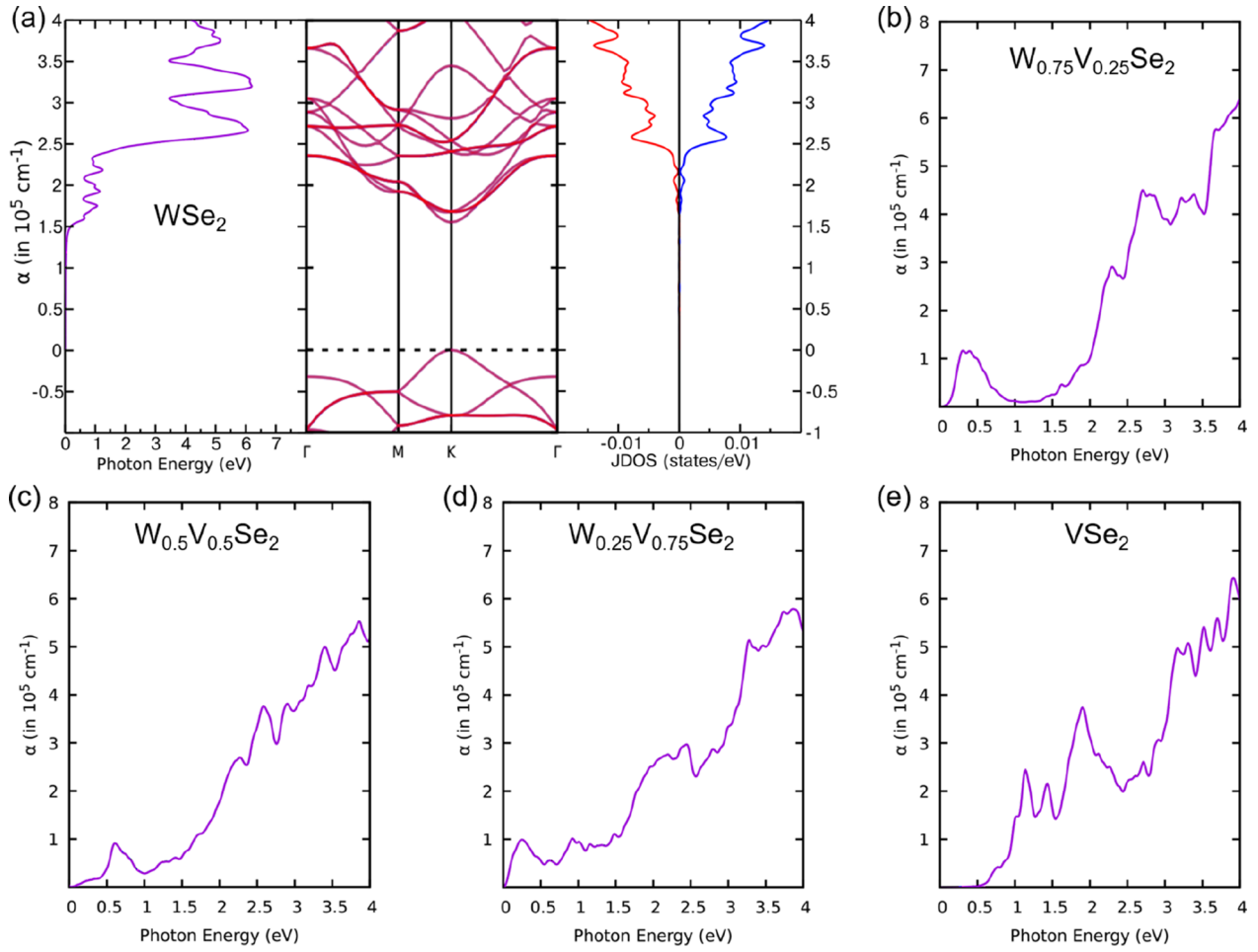

Figure 8. (a) Absorption coefficient, E-k diagram and joint density of states (JDOS) for WSe_2. For the E-k diagram, VBM at K point is set to zero energy. Absorption coefficient for (b) $W_{0.75}V_{0.25}Se_2$, (c) $W_{0.5}V_{0.5}Se_2$, (d) $W_{0.25}V_{0.75}Se_2$, and (e) VSe_2.

Magnetism distribution of pristine WSe_2, VSe_2, and their alloy compositions was estimated from charge distribution as can be seen in Figure 7. For WSe_2, total magnetization was found to be zero. Hence, magnetism distribution in Figure 7b does not show any spin polarization around the atoms. For $W_{0.75}V_{0.25}Se_2$, only the V atom possessed significant atomic magnetic moment which can be seen from the spin polarization plot in Figure 7c. For $W_{0.5}V_{0.5}Se_2$ and $W_{0.25}V_{0.75}Se_2$, V atoms induced an atomic magnetic moment in W atoms in the same direction of the spin polarization of V atoms. For pristine VSe_2, magnetism distribution showed atomic magnetic moments of V atoms are ferromagnetically ordered, which was consistent with previous report .[10] Figure 7 also shows change in induced magnetization with the increase in composition of vanadium. Total magnetic moment of V atoms closely followed the total magnetization curve. Thus, in all the alloy compositions and pristine VSe_2, magnetization mostly originated from atomic magnetic moments of the V atoms.

Top view of charge density difference for WSe_2, VSe_2, $W_{0.75}V_{0.25}Se_2$, $W_{0.5}V_{0.5}Se_2$, and $W_{0.25}V_{0.75}Se_2$ alloys are shown in the Supporting Information (see Figure S7). Unlike the pristine structures, the $W_{0.75}V_{0.25}Se_2$ alloy showed an anisotropic behavior in the charge density difference. Though there were regions of depletion around V atoms in pristine VSe_2, for the same isosurface value, the V atom in $W_{0.75}V_{0.25}Se_2$ did not show same region of depletion around itself. In case of $W_{0.5}V_{0.5}Se_2$ and $W_{0.25}V_{0.75}Se_2$, this anisotropic behavior was increased further and new regions of charge accumulation was seen around the V atoms.

Table 5 shows average charge transfer of V, Se, and W atoms in the crystal structures as calculated through Bader charge analysis. It was seen that, charge transfer to Se atoms increased as the composition of V atoms were increased in the alloys. This effect can be attributed to Se layers moving inward to the transition metal layer with alloying as stated before. Charge transfer from V atoms showed less changes compared to Se and W atoms. However, charge density difference plots (Figure S7c−e) showed spatial charge redistribution around the V atoms.

Optical properties of $W_{1-x}V_xSe_2$ alloy monolayers for different compositions were calculated. Calculation details are provided in the Supporting Information. Real and imaginary parts of the complex dielectric constant for pristine monolayers and their consequent alloys are presented in Figure S11 of the Supporting Information. Frequency-dependent refractive index, n, and extinction coefficient, κ, were determined from the complex dielectric constant. The absorption coefficient, α, was determined from the equation, $\alpha = 4\pi\kappa/\lambda$, where λ is the wavelength of the incident photon. The absorption coefficient, E-k diagram and JDOS for pristine WSe_2 is presented in Figure 8a. Under 1.55 eV, JDOS was close to zero. The absorption edge was found at around 1.55 eV which corresponds to the direct band gap of WSe_2 at K point. α depends on the quantum-mechanical probability of electron transition from filled states of

https://doi.org/10.1021/acsomega.2c03312
ACS Omega 2022, 7, 36184−36194

the valence band to empty states of the conduction band. From JDOS, we get the total picture of number of occupied states at E and unoccupied states at $E + h\nu$, where $h\nu$ is the photon energy. Absorption peaks found at higher energy matched with the peaks found in JDOS. For WSe_2, there was a steep increase in α at 2.5 eV. It was due to interband transitions into higher energy levels of the conduction band. $W_{0.75}V_{0.25}Se_2$ and $W_{0.25}V_{0.75}Se_2$ possessed a substantial amount of α in infrared range, as shown in Figure 8. These two alloys also showed the Reststrahlen effect in this range which is described in the Supporting Information. For $W_{0.5}V_{0.5}Se_2$, an absorption edge was found above 0.5 eV. This was due to direct transition between the highest occupied spin-up state and the lowest unoccupied spin-down state at the Γ point. These two bands were parallel and showed similar curvature around the Γ point. A gap of 0.54 eV was present between the bands. The absorption edge for VSe_2 above 0.67 eV was due to direct transition from the highest occupied spin-up band to the lowest unoccupied spin-up band at the K point. Pristine WSe_2 and VSe_2 showed large absorption in the visible light region but the absorption coefficient dropped in the infrared region. However, the alloys showed good absorption both in the infrared region and the visible light region.

4. CONCLUSIONS

We studied the effects of alloying on structural, electronic, optical, and magnetic properties of monolayer $W_{1-x}V_xSe_2$ using DFT calculations. Alloying the 1H-WSe_2 monolayer with 1H-VSe_2 monolayer introduced changes in the crystal structure and lattice parameter was increased. Because of alloying, a transition from semiconducting (WSe_2) to metallic ($W_{1-x}V_xSe_2$) to semiconducting (VSe_2) state was observed. All of the alloys demonstrated induced magnetism. Total magnetic moment increased with the increase of vanadium composition and maximum magnetic moment of 4.0 μ_B/(V_4Se_8 supercell) was reached for VSe_2. By investigating the spin polarization, the pristine 1-H VSe_2 monolayer and all the monolayer alloys were found to be ferromagnetically ordered. $W_{0.25}V_{0.75}Se_2$ alloy showed unique spin filtering characteristics. In $W_{0.25}V_{0.75}Se_2$, a gap of 0.8 eV opened for the spin-up channel, while the spin-down channel showed no gap around the Fermi level. Because of this barrier, 42% spin polarization was found in the tunnel current without incorporation of SOC. Below the Curie temperature, electrical conductivity for the spin-down channel was around 10^{19} $(\Omega\ cm\ s)^{-1}$, while the spin-up channel showed zero electrical conductivity when the chemical potential was 0.2 eV above the Fermi energy. These properties can be exploited to create spin filter tunnel junctions in spin filtering transistors. Investigation of the optical properties revealed good absorption of alloy monolayers in the infrared region which was not present in pristine WSe_2 and VSe_2 monolayers. Our results will provide direction for utilizing FM monolayer TMD alloys which could be useful in designing novel spin-electronic devices.

■ ASSOCIATED CONTENT

Supporting Information

The Supporting Information is available free of charge at https://pubs.acs.org/doi/10.1021/acsomega.2c03312.

Dynamical stability of pristine VSe_2 and monolayer alloys; band diagram of $W_{0.25}V_{0.75}Se_2$ with and without SOC; total magnetization with and without SOC; orbital projected band diagram and density of states for d orbitals of W and V atoms in $W_{0.75}V_{0.25}Se_2$ and s, p orbitals of Se, W, and V atoms in pristine WSe_2, pristine VSe_2, and monolayer alloys; molecular orbitals for WSe_2, VSe_2, and $W_{0.25}V_{0.75}Se_2$; charge density difference isosurfaces; ground state magnetic order; Curie temperature calculation; details of electrical conductivity calculation; and complex dielectric constant, complex reflective index, transmittance, and reflectance of pristine and alloy monolayers (PDF)

■ AUTHOR INFORMATION

Corresponding Author

Ahmed Zubair − *Department of Electrical and Electronic Engineering, Bangladesh University of Engineering and Technology, Dhaka 1205, Bangladesh;* orcid.org/0000-0002-1833-2244; Email: ahmedzubair@eee.buet.ac.bd

Author

Khondker Shihabul Hoque − *Department of Electrical and Electronic Engineering, Bangladesh University of Engineering and Technology, Dhaka 1205, Bangladesh;* orcid.org/0000-0002-0302-0563

Complete contact information is available at: https://pubs.acs.org/10.1021/acsomega.2c03312

Notes

The authors declare no competing financial interest.

■ ACKNOWLEDGMENTS

The authors acknowledge the facility and the support provided by the department of Electrical and Electronic Engineering, Bangladesh University of Engineering and Technology.

■ REFERENCES

(1) Lembke, D.; Kis, A. Breakdown of High-Performance Monolayer MoS_2 Transistors. *ACS Nano* **2012**, *6*, 10070−10075.

(2) Zhang, Y. J.; Oka, T.; Suzuki, R.; Ye, J. T.; Iwasa, Y. Electrically Switchable Chiral Light-Emitting Transistor. *Science* **2014**, *344*, 725−728.

(3) Wang, Q. H.; Kalantar-Zadeh, K.; Kis, A.; Coleman, J. N.; Strano, M. S. Electronics and optoelectronics of two-dimensional transition metal dichalcogenides. *Nat. Nanotechnol.* **2012**, *7*, 699−712.

(4) Baugher, B. W. H.; Churchill, H. O. H.; Yang, Y.; Jarillo-Herrero, P. Optoelectronic devices based on electrically tunable p-n diodes in a monolayer dichalcogenide. *Nat. Nanotechnol.* **2014**, *9*, 262−267.

(5) Liu, Y.; Gao, Y.; Zhang, S.; He, J.; Yu, J.; Liu, Z. Valleytronics in transition metal dichalcogenides materials. *Nano Res.* **2019**, *12*, 2695−2711.

(6) Ifti, I. M.; Hasan, M. M.; Arif, M. A. H.; Zubair, A.Effect of Vacancy on Electronic Properties of MX_2 (M = Mo, W and X = S, Se) Monolayers. In *2020 11th International Conference on Electrical and Computer Engineering (ICECE)*; , 2020, pp 391−394.

(7) Yang, D.; Fan, X.; Zhang, F.; Hu, Y.; Luo, Z. Electronic and Magnetic Properties of Defected Monolayer WSe_2 with Vacancies. *Nanoscale Res. Lett.* **2019**, *14*, 192.

(8) Zhao, S.; Tao, L.; Miao, P.; Wang, X.; Liu, Z.; Wang, Y.; Li, B.; Sui, Y.; Wang, Y. Strong room-temperature emission from defect states in CVD-grown WSe_2 nanosheets. *Nano Res.* **2018**, *11*, 3922−3930.

(9) Spiecker, E.; Schmid, A. K.; Minor, A. M.; Dahmen, U.; Hollensteiner, S.; Jäger, W. Self-Assembled Nanofold Network Formation on Layered Crystal Surfaces during Metal Intercalation. *Phys. Rev. Lett.* **2006**, *96*, 086401.

(10) Li, F.; Tu, K.; Chen, Z. Versatile Electronic Properties of VSe_2 Bulk, Few-Layers, Monolayer, Nanoribbons, and Nanotubes: A Computational Exploration. *J. Phys. Chem. C* **2014**, *118*, 21264−21274.

(11) Zhang, F.; et al. Monolayer Vanadium-Doped Tungsten Disulfide: A Room-Temperature Dilute Magnetic Semiconductor. *Adv. Sci.* **2020**, *7*, 2001174.
(12) Song, B.; Yun, S. J.; Jiang, J.; Avila, J.; Beach, K.; Choi, W.; Kim, Y.-M.; Yoon, D.; Terrones, H.; Song, Y. J.; Asensio, M. C.; Duong, D. L.; Lee, Y. H. Evidence of itinerant holes for long-range magnetic order in the tungsten diselenide semiconductor with vanadium dopants. *Phys. Rev. B* **2021**, *103*, 094432.
(13) Solanki, G.; Pataniya, P.; Sumesh, C.; Patel, K.; Pathak, V. Excitonic emission and absorption resonances in $V_{0.25}W_{0.75}Se_2$ single crystals grown by direct vapour transport technique. *J. Cryst. Growth* **2016**, *441*, 101−106.
(14) Pataniya, P.; Solanki, G. K.; Patel, K. D.; Pathak, V. M.; Sumesh, C. K. Crystal growth, characterization and photo detection properties of 2H-$V_{0.75}W_{0.25}Se_2$ ternary alloy with 1T-VSe_2 secondary phase. *Mater. Res. Express* **2017**, *4*, 106306.
(15) Santos, T. S.; Moodera, J. S. Observation of spin filtering with a ferromagnetic EuO tunnel barrier. *Phys. Rev. B* **2004**, *69*, 241203.
(16) Sugahara, S.; Tanaka, M. A novel spin transistor based on spin-filtering in ferromagnetic barriers: a spin-filter transistor. *Phys. E* **2004**, *21*, 996−1001.
(17) Giannozzi, P.; Baroni, S.; Bonini, N.; Calandra, M.; Car, R.; Cavazzoni, C.; Ceresoli, D.; Chiarotti, G. L.; Cococcioni, M.; Dabo, I.; et al. QUANTUM ESPRESSO: a modular and open-source software project for quantum simulations of materials. *J. Phys.: Condens. Matter* **2009**, *21*, 395502.
(18) Giannozzi, P.; Andreussi, O.; Brumme, T.; Bunau, O.; Buongiorno Nardelli, M.; Calandra, M.; Car, R.; Cavazzoni, C.; Ceresoli, D.; Cococcioni, M.; et al. Advanced capabilities for materials modelling with Quantum ESPRESSO. *J. Phys.: Condens. Matter* **2017**, *29*, 465901.
(19) Marzari, N.; Vanderbilt, D.; De Vita, A.; Payne, M. C. Thermal Contraction and Disordering of the Al(110) Surface. *Phys. Rev. Lett.* **1999**, *82*, 3296−3299.
(20) Schutte, W.; De Boer, J.; Jellinek, F. Crystal structures of tungsten disulfide and diselenide. *J. Solid State Chem.* **1987**, *70*, 207−209.
(21) Henkelman, G.; Arnaldsson, A.; Jónsson, H. A fast and robust algorithm for Bader decomposition of charge density. *Comput. Mater. Sci.* **2006**, *36*, 354−360.
(22) Madsen, G. K.; Singh, D. J. BoltzTraP. A code for calculating band-structure dependent quantities. *Comput. Phys. Commun.* **2006**, *175*, 67−71.
(23) Dyson, F. J. The S Matrix in Quantum Electrodynamics. *Phys. Rev.* **1949**, *75*, 1736−1755.
(24) Sangalli, D.; Ferretti, A.; Miranda, H.; Attaccalite, C.; Marri, I.; Cannuccia, E.; Melo, P.; Marsili, M.; Paleari, F.; Marrazzo, A.; et al. Many-body perturbation theory calculations using the yambo code. *J. Phys.: Condens. Matter* **2019**, *31*, 325902.
(25) Wei, X.-L.; Zhang, H.; Guo, G.-C.; Li, X.-B.; Lau, W.-M.; Liu, L.-M. Modulating the atomic and electronic structures through alloying and heterostructure of single-layer MoS_2. *J. Mater. Chem. A* **2014**, *2*, 2101−2109.
(26) Zeng, H.; Liu, G.-B.; Dai, J.; Yan, Y.; Zhu, B.; He, R.; Xie, L.; Xu, S.; Chen, X.; Yao, W.; Cui, X. Optical signature of symmetry variations and spin-valley coupling in atomically thin tungsten dichalcogenides. *Sci. Rep.* **2013**, *3*, 1608.
(27) Kang, J.; Tongay, S.; Zhou, J.; Li, J.; Wu, J. Band offsets and heterostructures of two-dimensional semiconductors. *Appl. Phys. Lett.* **2013**, *102*, 012111.
(28) Pan, H. Electronic and Magnetic Properties of Vanadium Dichalcogenides Monolayers Tuned by Hydrogenation. *J. Phys. Chem. C* **2014**, *118*, 13248−13253.
(29) Simmons, J. G. Generalized Formula for the Electric Tunnel Effect between Similar Electrodes Separated by a Thin Insulating Film. *J. Appl. Phys.* **1963**, *34*, 1793−1803.
(30) Moodera, J. S.; Hao, X.; Gibson, G. A.; Meservey, R. Electron-Spin Polarization in Tunnel Junctions in Zero Applied Field with Ferromagnetic EuS Barriers. *Phys. Rev. Lett.* **1988**, *61*, 637−640.
(31) Moodera, J. S.; Meservey, R.; Hao, X. Variation of the electron-spin polarization in EuSe tunnel junctions from zero to near 100% in a magnetic field. *Phys. Rev. Lett.* **1993**, *70*, 853−856.
(32) Turek, I.; Kudrnovsk, J.; Bihlmayer, G.; Blugel, S. Ab initiotheory of exchange interactions and the Curie temperature of bulk Gd. *J. Phys.: Condens. Matter* **2003**, *15*, 2771−2782.

https://doi.org/10.1021/acsomega.2c03312
ACS Omega 2022, 7, 36184−36194